Towards photocatalytic water splitting in homogeneous solutions using molecular metalloporphyrin photosensitizers and catalysts

Liu, C.

2

Ligand Controls the Activity of Light-driven Water Oxidation Catalyzed by Ni(II)-porphyrin Complexes in Neutral Homogeneous Aqueous Solutions

Finding photostable, first-row transition metal-based molecular systems for photocatalytic water oxidation is a step towards sustainable solar fuel production. This chapter discovered that nickel(II) hydrophilic porphyrins are molecular catalysts for photocatalytic water oxidation in neutral to acidic aqueous solutions using $[Ru(bpy)_3]^{2+}$ *as photosensitizer and* $[S_2O_8]^{2-}$ *as sacrificial electron acceptor. Electron-poorer Ni-porphyrins bearing 8 fluorine or 4 methylpyridinium substituents as electron-poorer porphyrins afforded 6-fold higher turnover frequencies (TOFs; ca. 0.65* min^{-1}*) than electronricher analogues. However, the electron-poorest Ni-porphyrin bearing 16 fluorine substituents was photocatalytically inactive under such conditions, because the potential at which catalytic* O_2 *evolution starts was too high (+1.23 V vs. NHE) to be driven by the photochemically generated* $[Ru(bpy)_3]^{3+}$*. Critically, these Ni-porphyrin catalysts showed excellent stability in photocatalytic conditions, as a second photocatalytic run replenished with a new dose of photosensitizer, afforded only 1–3% less* O_2 *than during the first photocatalytic run. Overall, optimizing the balance between the overpotential of the water oxidation catalyst and the driving force of electron transfer between the catalyst and the photogenerated oxidant* $[Ru(bpy)_3]^{3+}$*, appears as critical for photocatalytic water oxidation kinetics.*

This chapter was published as a research article: C. Liu, D. van den Bos, B. den Hartog, D. van der Meij, A. Ramakrishnan, S. Bonnet, *Angew. Chem. Int. Ed.* **2021**, *60*, 13463-13469.

2.1 Introduction

Photochemical water oxidation plays a critical role in artificial photosynthesis and solar fuel production, as water represents the most sustainable source of electrons for CO_2 and proton reduction.[1-10] In particular, molecular water-oxidation catalysts capable of generating O_2 in homogeneous conditions and under the action of light have generated great attention, because they form the basis for integrated supramolecular solar-fuel generating devices. In principle, such molecular complexes offer fascinating possibilities of varying the ligands with atomic precision, which allows for fine-tuning the coordination sphere and electron density of the metal-based catalyst, to optimize catalytic efficacy.[11,12] However, many molecular catalysts that were initially developed to act as molecules in photocatalytic water oxidation systems, were later shown to decompose in the harsh conditions of photocatalytic water oxidation into metal oxides, which are themselves catalytically active in the oxygen-evolution reaction (OER). It is hence critical to demonstrate the stability of a molecular catalyst in photocatalytic conditions, before claiming that it is catalytically active as a molecule.

Although molecular catalysts based on ruthenium or iridium still offer the highest stabilities and activities for photocatalytic water oxidation to date,[13-16] recently those made of first-row transition metals such as V,[17,18] Mn,[18,19] Fe,[20,21] Co,[22-35] and Cu[36,37] have received increased attention because of their lower cost and greater abundance on earth. However, most of them are only active in alkaline environment, which is sub-optimal for photocatalytic solar fuel generation systems combining water oxidation and either proton or CO_2 reduction, which typically require more neutral or even acidic (CO_2-saturated) conditions. Nickel is earth-abundant as well, and a number of Ni(II) complexes have been recently proposed as molecular catalysts for electrocatalytic OER,[38-41] where they showed high activities in pH-neutral aqueous solutions. However, molecular nickel-based water oxidation catalysts remain rare in artificial photosynthesis.[11] There is to our knowledge no demonstration of the use of Ni(II) complexes for the OER in photocatalytic conditions, with the exception of a report from Chen et al,[41] showing photocatalytic water oxidation with Ni-based precursor complexes that clearly serve as pre-catalysts that become active only after decomposition into Ni oxide.

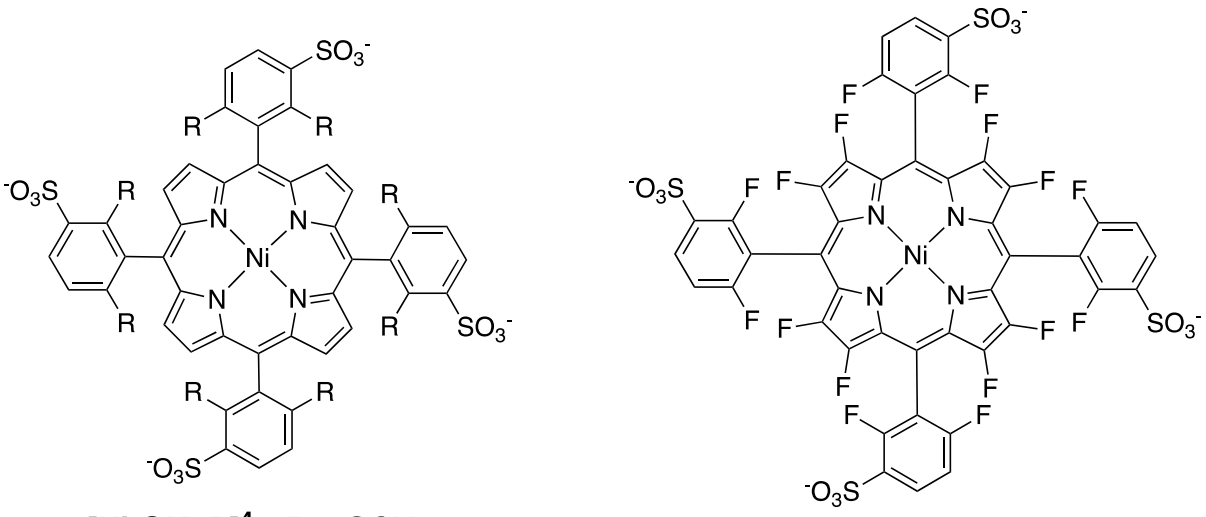

Figure 2.1 *Chemical structures of water soluble Ni(II)-porphyrin complexes used in this work, isolated with Na^+ counter ions.*

Herein, we report a series of four tetraanionic Ni(II)-porphyrin complexes bearing either electron-donating ([Ni-OMeP]$^{4-}$, [Ni-MeP]$^{4-}$) or electron-withdrawing ([Ni-F8P]$^{4-}$, [Ni-F16P]$^{4-}$) substituents (Figure 2.1). These catalysts were found to be active in the photocatalytic OER in homogeneous aqueous solutions in presence of $[Ru(bpy)_3]Cl_2$ as photosensitizer (PS), $Na_2S_2O_8$ as sacrificial electron acceptor (EA), blue light (450 nm), and at neutral to acidic pH. The four substitution patterns, from electron-rich [Ni-OMeP]$^{4-}$ to the electron poor [Ni-F16P]$^{4-}$, were designed based on the simplified photocatalytic mechanism for water oxidation shown in Figure 2.2. In Step 1, the photosensitizer PS absorbs a photon and is excited to an excited state that transfers an electron to $[S_2O_8]^{2-}$ to afford PS^+ ($[Ru^{III}(bpy)_3]^{3+}$), SO_4^{2-}, and a $SO_4^{\bullet-}$ radical that subsequently oxidizes a second equivalent of PS to PS^+ (Figure AI.1).[42,43] In Step 2, PS^+ oxidizes with an electron-transfer driving force E_{df} the water oxidation catalyst (Cat) to Cat^+, which, after several repetitions of the same process, affords higher oxidation states of the catalyst capable to catalytically oxidize water, which corresponds to Step 3. The driving force for this last step, usually referred to as the overpotential η, corresponds to the potential at which the catalyst turns over significantly, to afford O_2 and four protons. The exceptional stability of the nickel(II) catalysts presented here enabled us to study the influence of the electron-donating and -withdrawing substituents of the nickel complexes on its redox properties,[44] on the interplay between E_{df} and η, and to relate these redox properties to the overall performance of the photocatalytic system (Figure 2.2). Since the charge of the catalyst may affect the electron-

transfer rate of Step 2,[45] two known positively charged Ni(II)-porphyrin complexes 5,10,15,20-tetrakis(4-N-methylpyridyl)porphyrin-nickel(II) tetratriflate ([Ni-MPyP]$^{4+}$) 5,10,15,20-tetrakis(4-(N,N,N-trimethylammonio)phenyl)porphyrin-nickel(II) tetratriflate ([Ni-TMAP]$^{4+}$) were included in this study as well. The chemical structures of these compounds are shown in Figure AI.2. By interrogating the mechanism shown in Figure 2.2, we established a design principle on how η and E_{df} should be balanced to develop molecular catalysts that maximize the performance of photocatalytic water oxidation.

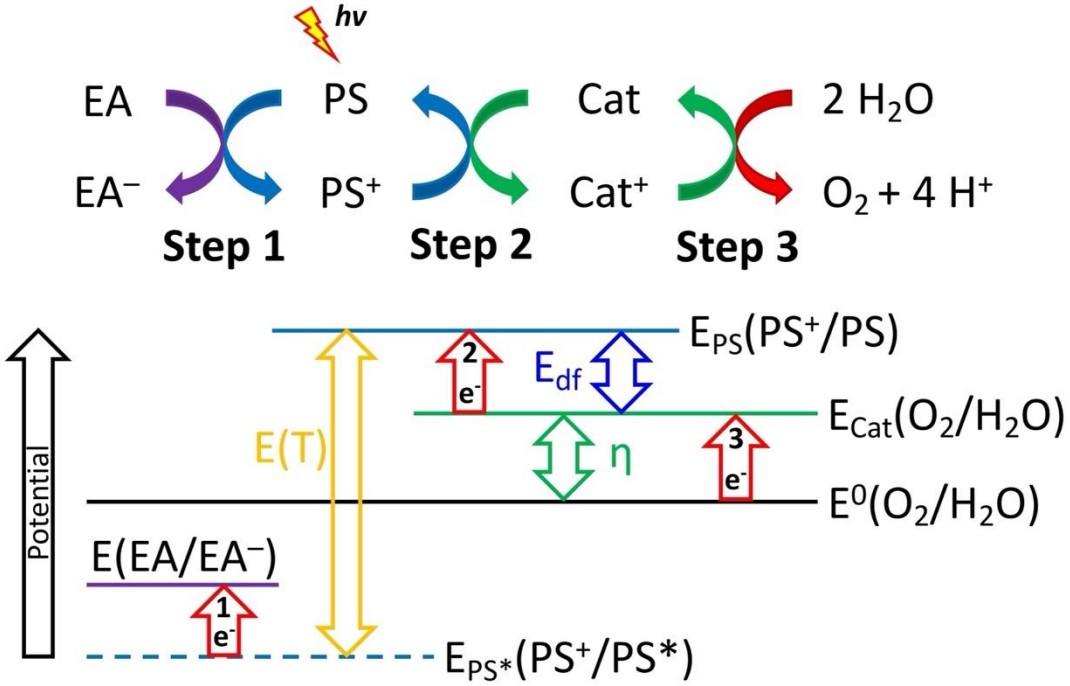

Figure 2.2 *Simplified photocatalytic mechanism and energy scheme of a three-component molecular homogeneous photocatalytic water oxidation system. EA: sacrificial electron acceptor; PS: photosensitizer; Cat: water oxidation catalyst; E(T): triplet exited state energy; η: overpotential of Cat; E_{df}: driving force of the electron transfer from the catalyst to the oxidized photosensitizer.*

2.2 Results and discussion

The tetrasulfonated porphyrin ligands [H_2-MeP]$^{4-}$, [H_2-F8P]$^{4-}$, and [H_2-F16P]$^{4-}$ were synthesized according to reported procedures,[46-50] while ligand [H_2-OMeP]$^{4-}$ was synthesized by sulfonation of 5,10,15,20-Tetrakis(2,6-dimethoxyphenyl)-21*H*,23*H*-porphyrin (OMeTPP using chlorosulfonic acid in anhydrous CH_2Cl_2 at room temperature. All four Ni(II) complexes were obtained by refluxing the free-base tetrasulfonatoporphyrin ligands with Ni(II) acetate in

Milli-Q water for 12 h under N_2. A Na^+-loaded ion-exchange resin was used to enforce the presence of Na^+ counter ions, and the complexes were finally purified by size-exclusion chromatography in order to remove the excess inorganic salts. The analytical purity of $[H_2\text{-OMeP}]^{4-}$, $[\text{Ni-OMeP}]^{4-}$, $[\text{Ni-MeP}]^{4-}$, $[\text{Ni-F8P}]^{4-}$ and $[\text{Ni-F16P}]^{4-}$, isolated to Na^+ salt, was established by NMR spectroscopy (Figure AI.3-10), high-resolution mass spectrometry, and elemental analysis.

In photocatalytic conditions using $[Ru(bpy)_3]Cl_2$ as the PS, $Na_2S_2O_8$ as EA, and blue light irradiation (450 nm), most molecular nickel catalysts tested in this study were found to produce O_2, but the oxygen evolution performances of the electron-poor nickel complexes $[\text{Ni-F8P}]^{4-}$ and $[\text{Ni-MPyP}]^{4+}$ were found to be significantly better than that of the relatively electron-rich complexes $[\text{Ni-OMeP}]^{4-}$ and $[\text{Ni-MeP}]^{4-}$ (Figure 2.3). Quite surprisingly, the electron-poorest complex, $[\text{Ni-F16P}]^{4-}$, showed no photocatalytic activity at all in these conditions, while nickel(II) acetate ($Ni(OAc)_2$), used as control, showed very low photocatalytic activity. This last result suggests that the homogeneous $[Ni(OH_2)_6]^{2+}$ ions or potential nickel oxide nanoparticles derived from decomposition of these ions in photocatalytic conditions are not active.

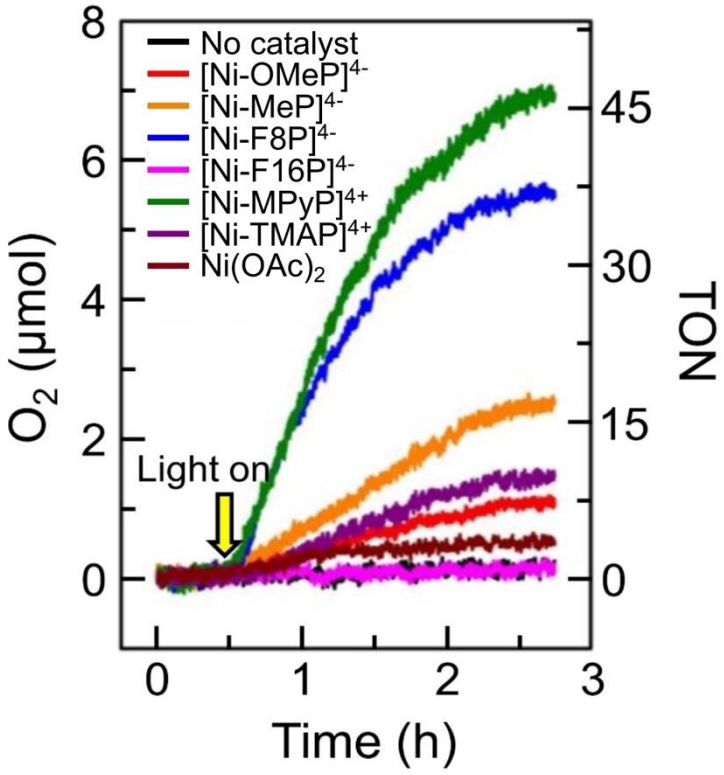

Figure 2.3 *Dioxygen evolution during photocatalytic water oxidation in presence of 0.05 mM catalyst [Ni-OMeP]$^{4-}$, [Ni-MeP]$^{4-}$, [Ni-F8P]$^{4-}$, [Ni-F16P]$^{4-}$, [Ni-MPyP]$^{4+}$, [Ni-TMAP]$^{4+}$, or $Ni(OAc)_2$, using 0.67 mM $[Ru(bpy)_3]Cl_2$ as photosensitizer, 50 mM $Na_2S_2O_8$ in 0.1 M pH 7.0 sodium phosphate buffer, and LED lamp (450 nm, 15.8 mW) for irradiation. T = 298 K.*

Considering the interesting photocatalytic activity of some of the Ni-porphyrin complexes, it was essential to test whether these compounds are catalytically active as homogeneous molecular species, or simply are pre-catalysts that decompose to nickel oxide nanoparticles, which have been shown repeatedly to catalyze the OER.[41] Several experiments were realized to investigate this question. First, phosphate-buffered solutions of each Ni-porphyrin complex at pH 7.0 were irradiated with blue light (450 nm, 15.8 mW) and their UV-vis spectrum was monitored in time during 3 h. The spectra did not change during irradiation (Figure AI.11-16), showing the intrinsic photostability of these molecules in absence of electron acceptor and photosensitizer. Second, dynamic light scattering (DLS) analysis was performed for full photocatalytic mixtures containing, next to PS and $Na_2S_2O_8$, either a Ni-porphyrin complex or $Ni(OAc)_2$. From these measurements we concluded that NiO_x nanoparticles were not formed when photocatalysis was realized at an initial neutral pH (7.0) and run for 0.5, 1.0, 1.5, or 2.0 h. As a positive control, photocatalytic experiments using $Ni(OAc)_2$ as the catalyst but realized at an initial basic pH (8.5), did show significant formation of NiO_x nanoparticles (Figure 2.4a). Hence, in the photocatalytic conditions of the experiments shown in Figure 2.3 none of the Ni(II)-porphyrin catalysts decomposed into nickel oxide nanoparticles. In a third experiment, after a first 2.75 h photocatalytic run with [Ni-F8P]$^{4-}$ for example, the photocatalytic mixture was clearly deactivated and did not produce O_2 anymore; the final pH was significantly reduced (typically ~2.8) and the TON was 36.5. O_2 production resumed with very similar rates as during the first photocatalytic run after neutralization of this solution by addition of NaOH, as well as a new batch of photosensitizer and of $Na_2S_2O_8$, and irradiated further in the same conditions (Figure 2.4b). After 2.25 h light irradiation the final O_2 evolution for [Ni-MPyP]$^{4+}$ was only 7% lower than in the first run, and for [Ni-OMeP]$^{4-}$, [Ni-MeP]$^{4-}$, [Ni-F8P]$^{4-}$, and [Ni-TMAP]$^{4+}$ loss of activity was only 1-3% (see Figure 2.4b for [Ni-F8P]$^{4-}$, and Figure AI.17 for [Ni-OMeP]$^{4-}$, [Ni-MeP]$^{4-}$, [Ni-MPyP]$^{4+}$and [Ni-TMAP]$^{4+}$).

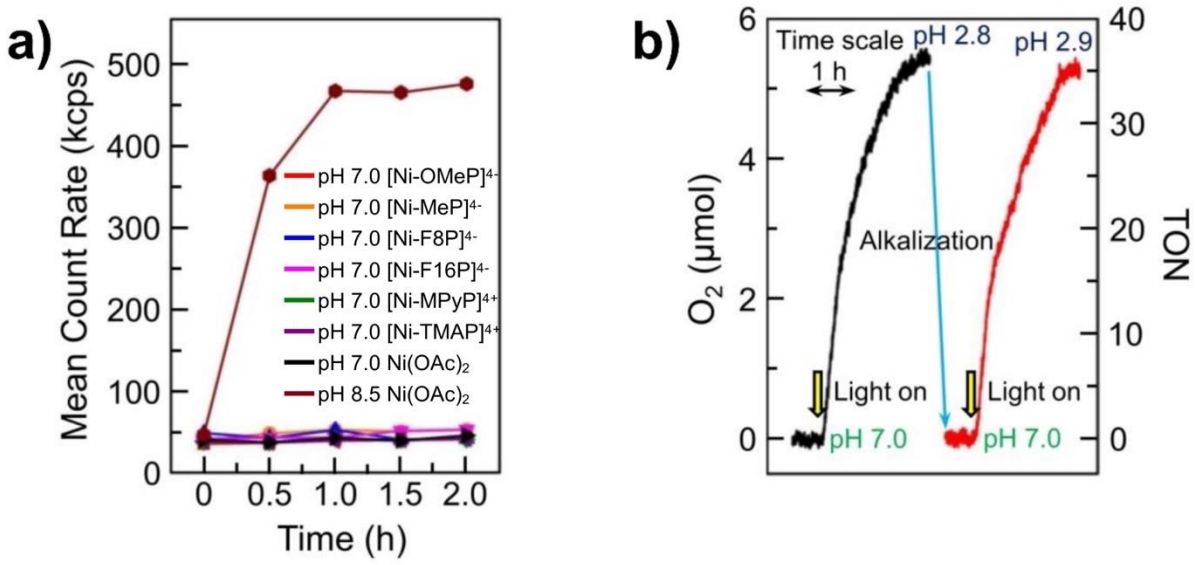

Figure 2.4 *a) Dynamic light scattering analysis after various times of photocatalytic water oxidation with different catalysts. Conditions: 50 mM $Na_2S_2O_8$, 0.67 mM $[Ru(bpy)_3]Cl_2$ and 0.05 mM water oxidation catalyst $[Ni\text{-}OMeP]^{4-}$, $[Ni\text{-}MeP]^{4-}$, $[Ni\text{-}F8P]^{4-}$, $[Ni\text{-}F16P]^{4-}$, $[Ni\text{-}MPyP]^{4+}$, $[Ni\text{-}TMAP]^{4+}$, or $Ni(OAc)_2$ in 0.1 M pH 7.0 phosphate buffer, and 50 mM $Na_2S_2O_8$, 0.67 mM $[Ru(bpy)_3]Cl_2$ or 0.05 mM Ni-Ac in 0.1 M pH 8.5 phosphate buffer. Conditions: blue light (450 nm, 15.8 mW), T = 298 K. b) Repetitive photocatalytic water oxidation using a homogeneous mixture containing 0.05 mM $[Ni\text{-}F8P]^{4-}$ with 0.67 mM $[Ru(bpy)_3]Cl_2$ and 50 mM $Na_2S_2O_8$ in 0.1 M sodium phosphate buffer (initial pH 7.0), using blue light (450 nm, 15.8 mW), T = 298 K. Between the two irradiation experiments, the solution was neutralized by adding solid NaOH and checking pH, after which 2.0 µmol fresh $[Ru(bpy)_3]Cl_2$ and 150 µmol $Na_2S_2O_8$ were added as solids.*

As a side note, the pH change during Ni-catalyzed photocatalytic water oxidation is remarkable, but was reported before.[13] Actually, the pH change from 7.0 to 2.8 was also observed when irradiating, in the same conditions as above, a solution containing the Ru photosensitizer and $Na_2S_2O_8$ but deprived of Ni catalyst (Figure AI.18). The pH change in photocatalytic conditions can hence essentially be explained by photosensitizer decomposition. Ghosh *et al* reported that formic acid may form by oxidation of the bipyridine ligands when $[Ru(bpy)_3]^{3+}$ is dissolved in aqueous solutions.[51] We indeed found both acetic and formic acid by ^1H NMR analysis of a D_2O solution containing 0.67 mM $[Ru(bpy)_3]Cl_2$ and 50 mM $Na_2S_2O_8$ irradiated for 2.25 h with blue light (450 nm, 15.8 mW, Figure AI.19), which suggests that the reasons causing the pH decrease is at least partly due to the formation of small organic acids derived from oxidation of the bipyridine ligands of the photosensitizer. It was repeatedly

reported that $[Ru(bpy)_3]Cl_2$ is not photostable in aqueous photocatalytic conditions.[42] Such instability obviously explains the limited TON observed in Figure 2.3; one should note, however, that another possible consequence of a lowered pH could be catalyst inactivation, because for some water oxidation catalysts (WOCs) the onset oxidation potential of the catalyst may shift upwards at lower pH.[13] The cyclic voltammetry (CV) and differential pulse voltammetry (DPV) of Ni-F8 at pH 2.8 (Figure AI.20) showed that OER indeed starts at a higher potential at pH 2.8 (+1.24 V vs. NHE) than at pH 7.0 (+1.12 V vs. NHE), but that the catalyst is still active for the OER, even in such acidic conditions.

In presence of all four components of the photocatalytic system using the catalyst $[Ni\text{-}F8P]^{4-}$, a second photocatalytic run realized after adding fresh PS showed good activity (Figure AI.21). This experiment suggested that photosensitizer decomposition is the main reason for the loss of photocatalytic activity, while the $[Ni\text{-}F8P]^{4-}$ catalyst could indeed cope with the lower pH 2.8 obtained at the end of the first photocatalytic run. In addition, the second photocatalytic run was limited by the low concentration of $Na_2S_2O_8$ remaining in the solution after the first photocatalytic run. Indeed, adding only a new batch of fresh PS to the deactivated solution, did not reactivate the system, while after adding another batch of fresh $Na_2S_2O_8$ as well, the system evolved O_2 for a third time, demonstrating the good stability of the catalyst. In this photocatalytic system, the depletion of photosensitizer and electron acceptor were the main reasons that limited the turnover numbers. Overall, this series of Ni-porphyrin complexes show great photostability not only in absence of photosensitizer and electron acceptor, but also in full photocatalytic conditions. This stability is in great contrast with that of for example $[Ru(bda)(isoq)_2]$ (H_2bda = 2,2′-bipyridine-6,6′-dicarboxylic acid; isoq = isoquinoline), which decomposes in parallel with the $[Ru(bpy)_3]^{2+}$ photosensitizer.[52] These results also demonstrate that the catalytic water-oxidation activity is indeed due to the presence of molecular species dissolved in a homogeneous solution, rather than nickel oxide nanoparticles.

As photocatalysis seems to be run by molecular species, it should be possible to correlate the (photo)catalytic activities to the molecular formulae of the complexes and the electron density of their metal centre. Their redox properties were hence determined by a combination of cyclic voltammetry (CV) and differential pulse voltammetry (DPV) in 0.1 M pH 7.0 phosphate buffer using a glassy-carbon (GC) electrode (Figure AI.22). According to the CV, the electron-rich complexes $[Ni\text{-}OMeP]^{4-}$ and $[Ni\text{-}MeP]^{4-}$ showed slower kinetics for the electrocatalytic OER than the electron-poor $[Ni\text{-}F8P]^{4-}$ and $[Ni\text{-}F16P]^{4-}$, as demonstrated by their lower catalytic current density compared with the blanks. Second, while $[Ni\text{-}OMeP]^{4-}$

showed a single DPV wave, all other complexes showed two waves, with electron-poor Ni-porphyrin complexes having higher DPV oxidation wave potentials. The second DPV wave is usually proposed as the potential at which electrocatalytic O_2 production actually starts.[1] To check this hypothesis, a controlled potential electrolysis (CPE) experiment was realized in a pH 7.0 phosphate-buffered solution using a system equipped with a Clark electrode for O_2 quantification. Using $[Ni\text{-}F8P]^{4-}$ (2 mM), a CPE experiment run at the potential of the first DPV wave (+0.98 V vs. NHE) did not evolve any oxygen. However, at the potential of the second DPV wave (+1.12 V vs. NHE) the solution indeed produced significant amounts of O_2 and the current was stable (Figure AI.23a-b). This observation suggests that the first oxidation of $[Ni\text{-}F8P]^{4-}$ results in the formation of oxidized species Ni^{II}-($por^{\bullet+}$) or Ni^{III}-por (por is the porphyrin ligand of $[Ni\text{-}F8P]^{4-}$) that is not able to catalyze water oxidation and hence can be reduced back to Ni^{II}-por, thus explaining the quasi-reversible redox process at $E_{1/2}$ = +0.98 V vs. NHE. Upon a second electron transfer at the potential of the second DPV wave, a catalytically active species is formed, which may be either Ni^{IV}-por or Ni^{III}-($por^{\bullet+}$).[1,39] No OER activity was observed when the GC electrode used in a first electrolytic run was rinsed with Milli-Q water and used in a second electrocatalytic run using fresh buffer (Figure AI.23c). In addition, the UV-vis spectra of the solution before and after CPE showed no difference (Figure AI.23d). Finally, the faradaic yield of the catalytic system, as determined in CPE was 95%±5%. Overall, Ni-F8 is hence stable in electrocatalytic conditions, and the oxygen evolution as determined in CPE is actually catalyzed by the molecular $[Ni\text{-}F8P]^{4-}$ complex, at the potential of the second DPV wave.

The complex $[Ni\text{-}F16P]^{4-}$ behaved quite differently. This electron-poor complex shows, as expected from the higher number of electron-withdrawing substituents, higher oxidation wave potentials in DPV (+1.23 and +1.42 V vs. NHE) than $[Ni\text{-}F8P]^{4-}$. However, in a 30 min CPE experiment, a 2 mM $[Ni\text{-}F16P]^{4-}$ solution electrocatalytically catalyzed the OER already at the first DPV wave potential (+1.23 V vs. NHE, see Figure AI.24) with a high faraidic yield (83±3%) showing that $[Ni\text{-}F16P]^{4-}$ forms a species that is active in OER upon one-electron oxidation. We speculate that this electron-poor species may catalyse water oxidation *via* a binuclear radical coupling mechanism,[53,54] and that the second DPV wave, which corresponds to further one-electron oxidation to Ni^{IV}-por or Ni^{III}-$por^{\cdot+}$, may catalyse water oxidation *via* a water nucleophilic attack, potentially with a higher energy barrier than the species formed by the first oxidation.[1,39] As a note, $[Ni\text{-}F16P]^{4-}$ is also stable during electrocatalytic OER according to UV-vis spectroscopy (Figure AI.24d). In photocatalytic conditions the photo-

oxidized sensitizer PS^+ ($[Ru(bpy)_3]^{3+}$) has only a very low driving force E_{df} = 30 mV to trigger hole transfer from PS^+ (+1.26 V vs. NHE) to the catalyst (+1.23 V vs. NHE), and photocatalysis does not take place. Thus, photocatalytic water oxidation can be driven by Ni(II)-porphyrin complexes provided that the redox properties of the catalyst find an optimum: the complex should have a DPV oxidation wave potential that is high enough to be able to drive water oxidation (Step 3 in Figure 2.2) at appreciable overpotential η, but it should be low enough to keep an appreciable driving force E_{df} for the photosensitizer to drive Step 2. In this photocatalytic system, an electron-transfer driving force E_{df} of 30 mV (for $[Ni\text{-}F16P]^{4-}$) is not high enough to drive photocatalysis, while an E_{df} of 140 mV (for $[Ni\text{-}F8P]^{4-}$) appears to be close to the optimum.

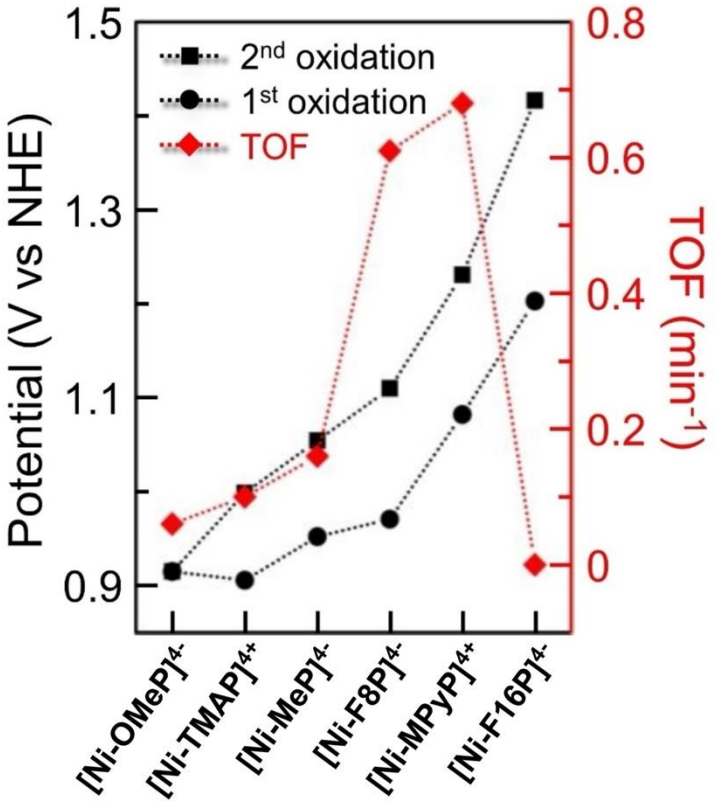

Figure 2.5 *DPV oxidation wave potentials (left axis, first and second oxidation shown by circles and squares, respectively) for $[Ni\text{-}OMeP]^{4-}$, $[Ni\text{-}MeP]^{4-}$, $[Ni\text{-}F8P]^{4-}$, $[Ni\text{-}F16P]^{4-}$, $[Ni\text{-}MPyP]^{4+}$, $[Ni\text{-}TMAP]^{4+}$, and maximun TOF (right axis, red diamonds, min^{-1}) obtained in the photocatalytic water oxidation experiments shown in Figure 2.3.*

Interestingly, the relative sign of the charge of the molecular catalyst and that of the photosensitizer were found to play a limited role in the relation between redox potentials and photocatalytic rates. Replacing a tetraanionic Ni-porphyrin catalyst by tetracationic Ni-

porphyrin complexes such as $[Ni\text{-}MPyP]^{4+}$ or $[Ni\text{-}TMAP]^{4+}$, did not introduce outliers in the trend discussed above (Figure 2.5). The potential of the second DPV oxidation wave of $[Ni\text{-}MPyP]^{4+}$ is slightly higher (0.12 V) than that of $[Ni\text{-}F8P]^{4-}$, but still lower than the redox potential of the $[Ru(bpy)_3]^{3+}/[Ru(bpy)_3]^{2+}$ couple, and indeed a slightly higher TOF was found in photocatalytic conditions for this complex. On the other hand, the potential of the second DPV oxidation wave of $[Ni\text{-}TMAP]^{4+}$ is lower than that of $[Ni\text{-}MeP]^{4-}$, and indeed a slightly lower TOF was found in photocatalysis. Hence it seems that in the series of nickel water-oxidation catalysts $[Ni\text{-}OMeP]^{4-}$, $[Ni\text{-}MeP]^{4-}$, $[Ni\text{-}F8P]^{4-}$, $[Ni\text{-}F16P]^{4-}$, $[Ni\text{-}MPyP]^{4+}$ and $[Ni\text{-}TMAP]^{4+}$, the electron-donating and -withdrawing nature of the porphyrin substituents is the main variable responsible for the variation in the photocatalytic efficiency, while the charge of the complex plays a minor role. Overall, $[Ni\text{-}F8P]^{4-}$ and $[Ni\text{-}MPyP]^{4+}$ were found to be the most active catalysts of this series of nickel complexes for photocatalytic OER. They offer the best compromise in terms of redox potential, i.e., an electrocatalytically active DPV oxidation wave potential that is high enough to maximize η and the rate of Step 3, but low enough for fast electron transfer to occur in Step 2 (Table AI.1).

As $[Ni\text{-}F8P]^{4-}$ appeared to be the most active catalyst for the series of new anionic complexes presented here, the mechanism of the photocatalytic OER in pH 7.0 phosphate buffer solution was further investigated. First, a first-order dependence of the O_2 evolution rate on catalyst concentration was observed using a fixed PS concentration of 0.67 mM (Figure 2.6a, 6b and Figure AI.25a), suggesting that the rate-determining step of the reaction involves a single nickel centre. Second, a first-order dependence of the O_2 evolution rate on PS concentration was found using a fixed $[Ni\text{-}F8P]^{4-}$ catalyst concentration of 50 µM (Figure 2.6c, 6d and Figure AI.25b), indicating that the rate-determining step of the photocatalytic system also involves one molecule of PS. Third, the TOF of the system is not significantly influenced by the photon flux when the light power is higher than 11 mW (Figure AI.26), showing that the photon density is in excess in such conditions, and that Step 1 does not limit the reaction rate. This result was confirmed by an experiment showing that there was very limited change of the rate of O_2 production when the concentration of $Na_2S_2O_8$ was varied in the range 25-100 mM (Figure AI.27). Finally, when $[Ru(bpy)_3](ClO_4)_3$ was used as chemical oxidant, the maximum O_2 evolution rate of the catalytic system was found to be linearly dependent on both the concentrations of $[Ru(bpy)_3]^{3+}$ and that of the $[Ni\text{-}F8P]^{4-}$ catalyst (Figure AI.28), suggesting that the role of the sulfate radical liberated by one-electron transfer from PS* to $S_2O_8^{2-}$, is minimal, i.e., that the photocatalytic O_2-evolution reaction is indeed driven by the

photochemical generation of $[Ru(bpy)_3]^{3+}$. Altogether, these results strongly suggest that under such photocatalytic conditions it is the electron transfer from the catalyst to the photo-oxidized photosensitizer PS^+, i.e. Step 2 in Figure 2.2, that is the rate-determining step of the photocatalytic system. This result, which is reminiscent of a study published by our group using Sun's catalyst $[Ru(bda)(isoq)_2]$,[52] is not only important mechanistically speaking; it also demonstrates that the $[Ni\text{-}F8P]^{4-}$ catalyst is fast enough for homogeneous photocatalytic water oxidation. Such a result is important because the catalytic activity of molecular water oxidation catalysts (hence the rate of Step 3) is often presented as the most important parameter to improve for achieving efficient production of solar fuels, while we here confirm that the rate of electron transfer can also be the bottleneck of the reaction. Assuming that only two photons are needed to produce four molecules of $[Ru(bpy)_3]^{3+}$ that can further be used to evolve one O_2 molecule, the quantum yield for O_2 production using 0.05 mM $[Ni\text{-}F8P]^{4-}$ as the catalyst, 0.67 mM $[Ru(bpy)_3]Cl_2$ as PS, 50 mM $Na_2S_2O_8$ as EA and 15.8 mW of blue light (450 nm), is 0.29%±0.05%. This modest value should be considered as strongly encouraging, as it is accompanied by an exceptional stability of the nickel catalysts in photocatalytic conditions, whereas decomposition of the photosensitizer and the depletion of peroxodisulfate limit the turnover number of the system.

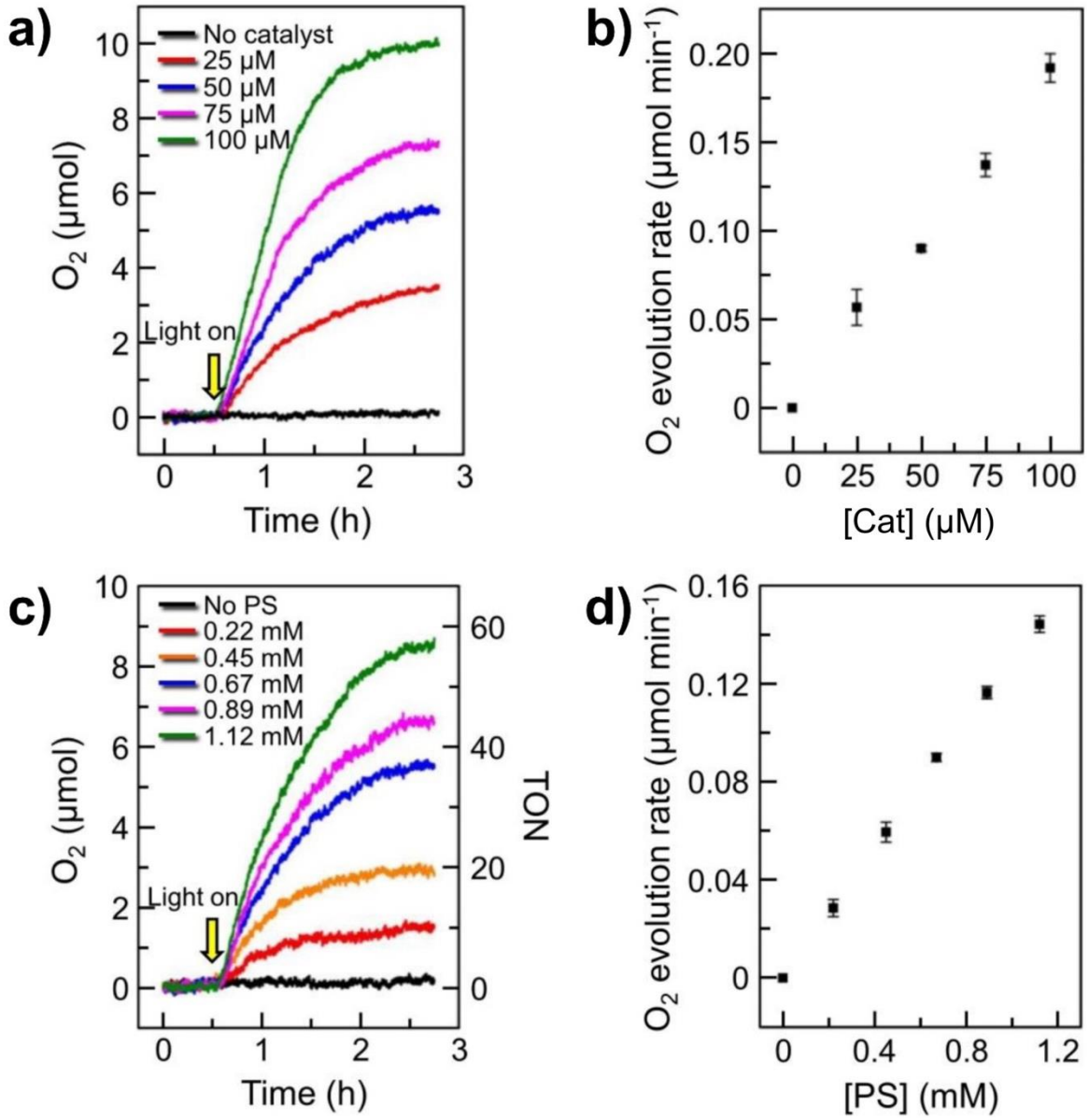

Figure 2.6 *Photocatalytic oxygen evolution vs. irradiation time with a) different concentrations of [Ni-F8P]$^{4-}$ with 0.67 mM [Ru(bpy)$_3$]Cl$_2$ as photosensitizer, and c) different concentrations of PS with 50 µM [Ni-F8P]$^{4-}$ as WOC. b) and d) maximum O$_2$ evolution rate during photocatalytic O$_2$ evolution plotted as a function of b) the concentration of [Ni-F8P]$^{4-}$ and d) the concentration of [Ru(bpy)$_3$]Cl$_2$. Conditions: 50 mM Na$_2$S$_2$O$_8$ in 0.1 M sodium phosphate buffer (initial pH 7.0), blue light (450 nm, 15.8 mW), T = 298 K.*

2.3 Conclusion

A series of four anionic Ni-porphyrin complexes was prepared that show promising catalytic properties for electrocatalytic and photocatalytic water oxidation in neutral to acidic phosphate-

buffered homogeneous aqueous solutions. Electrochemical studies revealed that modifications of the tetrasulfonatoporphyrin ligand with more electron-withdrawing substituents increased the potentials of the DPV oxidation waves, and strongly influenced the rate of the OER in photocatalytic conditions. A balance has to be found between increasing these oxidation potentials, which provide a higher driving force (η) for the nickel-catalyzed OER reaction itself, and lowering it, to keep the driving force for electron transfer from the catalyst to the oxidized photosensitizer PS^+ (E_{df}), high enough. $[Ni\text{-}F16P]^{4-}$, for example, is too electron-poor, which inactivates photocatalysis by blocking the electron transfer of Step 2. A photosensitizer with a higher oxidation potential than the $[Ru(bpy)_3]^{3+}/[Ru(bpy)_3]^{2+}$ couple may alleviate this problem and unravel the otherwise excellent electrocatalytic OER properties of this complex. By contrast, $[Ni\text{-}F8P]^{4-}$ and $[Ni\text{-}MPyP]^{4+}$ were found close to the optimum, at least for $[Ru(bpy)_3]^{2+}$ as photosensitizer, and offered excellent activity for the photocatalytic OER. Critically, these first-row transition metal complexes showed great stability both in photocatalytic and electrocatalytic conditions, and for $[Ni\text{-}F8P]^{4-}$ the TON of the photocatalytic system appeared to be limited predominantly by decomposition of the ruthenium photosensitizer. This work represents a significant advance in the field of solar fuel production, since it provides a rare example of homogeneous light-driven water oxidation catalyzed by Ni-based molecular catalyst, and this in neutral to acidic aqueous solutions. Last but not least, it provides a clear framework to design molecular catalysts for photocatalysis: the electron-density of the catalytic centre should be fine-tuned with appropriate substituents, to balance the driving forces of catalytic water oxidation vs. electron transfer from the catalyst to PS^+.

2.4 Experimental section

2.4.1 Materials and methods

All reagents were purchased from Sigma-Aldrich and used as received unless otherwise noted. The compounds 5,10,15,20-tetrakis(2,6-dimethoxyphenyl)-21*H*,23*H*-porphyrin (OMeTPP),[55] tetrasodium-5,10,15,20-tetrakis(2,6-dimethylphenyl-3-sulfonatophenyl)-21*H*,23*H*-porphyrin ($[H_2\text{-}MeP]^{4-}$),[56] tetrasodium-5,10,15,20-tetrakis(2,6-difluoro-3-sulfonatophenyl)-21*H*,23*H*-porphyrin ($[H_2\text{-}F8P]^{4-}$),[57] tetrasodium-2,3,7,8,12,13,17,18-octafluoro-5,10,15-20-tetrakis(2,6-difluoro-3-sulfonatophenyl)-21*H*,23*H*-porphyrin ($[H_2\text{-}F16P]^{4-}$),[58] 5,10,15,20-tetrakis(4-N-methylpyridyl)porphyrin-nickel(II) tetratriflate ($[Ni\text{-}MPyP]^{4+}$),[39,59] 5,10,15,20-tetrakis(4-(N,N,N-trimethylammonio)phenyl)porphyrin-nickel(II) tetratriflate ($[Ni\text{-}TMAP]^{4+}$),[59] and $[Ru(bpy)_3](ClO_4)_3$[60,61] were prepared according to

published methods. ^{1}H NMR spectra were recorded on a Bruker 400DPX-liq spectrometer operating at 400 MHz. ^{13}C NMR spectra and ^{19}F NMR spectra were recorded on a Bruker 500DPX spectrometer operating at 500 MHz. Mass spectra were obtained using a Finnigan Aqueous Mass Spectrometer (MS) with electrospray ionization (ESI) in negative ion mode. High-resolution mass spectrometric measurements were made on a Bruker Fourier Transform Ion Cyclotron Resonance Mass Spectrometer APEX IV at Leiden University. Elemental analyses were performed at the Mikroanalytisches Laboratorium Kolbe, Germany. Electronic absorption spectra were obtained on a Varian Cary 60 spectrophotometer at 25 °C during the spectrophotometric measurements. The LED optical power was measured using an OPHIR Nova-display laser power meter.

2.4.2 Synthesis

Tetrasodium 5,10,15,20-tetrakis(2,6-dimethoxyl-3-sulfonatophenyl)-21*H*,23*H*-porphyrin ($Na_4[H_2$-OMeP])

5,10,15,20-Tetrakis(2,6-dimethoxyphenyl)-21*H*,23*H*-porphyrin (85 mg, 0.10 mmol) and anhydrous CH_2Cl_2 (100 mL) were placed under N_2 in a 250 mL three-neck round-bottom flask equipped with a magnetic stirring bar and rubber stoppers. Chlorosulfonic acid (58 mg, 34 μL, 0.50 mmol) was injected into the stirred solution using a microsyringe and the reaction mixture was stirred for 3 h at room temperature. Water (100 mL) was then added to the solution and the water phase was collected using a separating funnel. A few drops of saturated aqueous $NaHCO_3$ solution were used to neutralize the solution to pH ≥ 8. The water was evaporated at 40 °C using a rotary evaporator and the residue was redissolved in cold methanol (20 mL). The solution was filtered over filter paper to remove excess $NaHCO_3$, and the solvent was evaporated. The crude product was then purified on a Sephadex-20H size exclusion chromatography column to remove remaining salts (eluent: methanol) and methanol was finally rotary evaporated and the solid dried in vacuo afforded $Na_4[H_2$-OMeP] as a dark red solid. Yield (115 mg, 91%); ^{1}H NMR (400 MHz, CD_3OD): δ = 8.85 (br, 8H; β-pyrrole-H), 8.41 (d, J = 9 Hz, 4H; *p*-Ph-H), 7.36 – 7.24 (m, 4H; *m*-Ph-H), 3.69, 3.67, 3.65, 3.64, 3.63, 3.61 (6 "s", ca. 1:2:1:1:2:1, 12H; OCH_3), 3.06, 3.00, 2.99, 2.96, 2.93, 2.87 ppm (6 "s", ca. 1:2:1:1:2:1, 12H; OCH_3); ^{13}C NMR (126 MHz, CD_3OD): δ = 163.9, 159.6, 132.2, 131.7, 127.0, 111.9, 106.7, 68.7, 62.3, 56.5, 27.0 ppm; MS (ESI neg. ion): *m*/*z* calcd for $C_{52}H_{42}N_4O_{20}S_4^{4-}$: 292.5 [*M*-4Na]$^{4-}$; found: 292.7; $C_{52}H_{42}N_4O_{20}S_4^{4-}+H^+$: 390.4 [*M*-4Na+H]$^{3-}$; found: 390.5; $C_{52}H_{42}N_4O_{20}S_4^{4-}+CH_3OH+H^+$: 401.1 [*M*-4Na+$CH_3$OH+H]$^{3-}$; found: 401.2; $C_{52}H_{42}N_4O_{20}S_4^{4-}+Na^+ +H^+$: 597.1

[*M*-3Na+H]$^{2-}$; found: 597.2; HRMS (ESI): *m*/*z* calcd for $C_{52}H_{47}N_4O_{20}S_4^+$: 1175.1661 [*M*-4Na+5H]$^+$; found: 1175.1665.

Tetrasodium 5,10,15,20-tetrakis(2,6-dimethoxyl-3-sulfonatophenyl)porphyrin nickel(II) (Na_4[Ni-OMeP])

The ligand $Na_4[H_2$-OMeP] (115 mg, 0.09 mmol) and Milli-Q water (40 mL) were placed under N_2 in a 100 mL round-bottom flask equipped with a magnetic stirring bar and a condenser. A solution of Ni(II) acetate tetrahydrate (112 mg, 0.45 mmol) in Milli-Q water (10 mL) was added to the stirred solution, and the mixture was refluxed for 12 h under N_2. After cooling to room temperature, water was rotary evaporated at 40 °C and the residue was redissolved in cold methanol (15 mL). After filtration on a filter paper, methanol was rotary-evaporated, the residue was redissolved in cold methanol (5 mL). The solution was filtered by filter paper, rotary-evaporated, and the crude product was redissolved in Milli-Q water (5 mL) then passed onto an Amberlite IR 120 Na^+ form ion exchange resin column (10 cm), washed with Milli-Q water and further purified on Sephadex-20H size exclusion chromatography to remove excess nickel acetate (methanol). Methanol was finally rotary evaporated and the solid dried in vacuo. Yield (113 mg, 89%); ^{1}H NMR (400 MHz, CD_3OD): δ = 8.82 – 8.65 (m, 8H; β-pyrrole-H), 8.36 – 8.32 (m, 4H; *p*-Ph-H), 7.33, 7.30, 7.23, 7.14 (4 "d", *J* = 9 Hz, ca. 1:3:3:1, 4H; *m*-Ph-H), 3.83 ("s"), 3.76 ("d"), 3.63 ("d"), 3.48 ("s") (ca. 1:3:3:1, 12 H; OCH_3), 3.24, 3.01, 2.99, 2.82, 2.75, 2.69 ppm (6 "s", ca. 1:1:2:2:1:1, 12 H; OCH_3); MS (ESI neg. ion): *m*/*z* calcd for $C_{52}H_{40}N_4NiO_{20}S_4^{4-}$: 306.5 [*M*-4Na]$^{4-}$; found: 306.7; $C_{52}H_{40}N_4NiO_{20}S_4^{4-}+H^+$: 409.0 [*M*-4Na+H]$^{3-}$; found: 409.2; $C_{52}H_{40}N_4NiO_{20}S_4^{4-}+CH_3OH+H^+$: 419.7 [*M*-4Na+$CH_3$OH+H]$^{3-}$; found: 419.8; $C_{52}H_{40}N_4NiO_{20}S_4^{4-}+2Na^+$: 636.0 [*M*-2Na]$^{2-}$; found: 636.1; HRMS (ESI): *m*/*z* calcd for $C_{52}H_{44}N_4NiO_{20}S_4Na^+$: 1153.0677 [*M*-3Na+4H]$^+$; found: 1153.0668; elemental analysis calcd (%) for $C_{52}H_{40}N_4Na_4NiO_{20}S_4 \cdot 5H_2O$: C 44.30, H 3.57, N 3.97; found: C 44.29, H 3.31, N 3.93. UV-vis (H_2O): $\lambda_{max}(\varepsilon)$ 409 nm (3.4×10^5), 525 nm (2.3×10^4), 558 nm (9.5×10^3 M^{-1} cm^{-1}).

Tetrasodium 5,10,15,20-tetrakis(2,6-dimethyl-3-sulfonatophenyl)porphyrin nickel(II) (Na_4[Ni-MeP])

Tetrasodium 5,10,15,20-tetrakis(2,6-dimethyl-3-sulfonatophenyl)-21*H*,23*H*-porphyrin·$9H_2O$ (130 mg, 0.10 mmol) and Milli-Q water (40 mL) were placed under N_2 in a 100 mL round-bottom flask equipped with a magnetic stirring bar and a condenser. A solution of Ni(II) acetate tetrahydrate (124 mg, 0.50 mmol) in Milli-Q water (10 mL) was added to the

stirred solution and the mixture was refluxed for 12 h under N_2. After cooling to room temperature, water was rotary evaporated and the residue was redissolved in cold methanol (15 mL). After filtration on a filter paper, methanol was rotary-evaporated, the residue was redissolved in cold methanol (5 mL), the solution was filtered a second time by filter paper and rotary-evaporated, then the crude product was then passed onto an Amberlite IR 120 Na^+ form ion exchange resin column (10 cm), washed with Milli-Q water and finally purified on Sephadex-20H size exclusion chromatography (methanol). Methanol was finally rotary evaporated and the solid dried in vacuo. Yield (120 mg, 92%); ^{1}H NMR (400 MHz, CD_3OD): δ = 8.60 – 8.57 (m, 8H; β-pyrrole-H), 8.33 – 8.29 (m, 4H; *p*-Ph-H), 7.52 – 7.47 (m, 4H; *m*-Ph-H), 2.38 – 2.23 (m, 12H; CH_3), 1.86 – 1.76 ppm (m, 12H; CH_3); MS (ESI neg. ion): *m*/*z* calcd for $C_{52}H_{41}N_4NiO_{12}S_4^{4-}+H^+$: 366.4 $[M\text{-}4Na+H]^{3-}$; found: 366.4; $C_{52}H_{40}N_4NiO_{12}S_4^{4-}+Na^+$: 373.7 $[M\text{-}3Na]^{3-}$; found: 373.9; $C_{52}H_{40}N_4NiO_{12}S_4^{4-}+2Na^+$: 572.0 $[M\text{-}2Na]^{2-}$; found: 572.3; HRMS (ESI): *m*/*z* calcd for $C_{52}H_{45}N_4NiO_{12}S_4^+$: 1103.1264 $[M\text{-}4Na+5H]^+$; found: 1103.1259; $C_{52}H_{43}N_4NiO_{12}S_4+2Na^+$: 1169.0723 $[M\text{-}2Na+3H]^+$; found: 1169.0732; elemental analysis calcd (%) for $C_{52}H_{40}N_4Na_4NiO_{12}S_4\cdot 6H_2O$: C 48.05, H 4.03, N 4.31; found: C 47.95, H 4.14, N 4.33. UV-vis (H_2O): $\lambda_{max}(\varepsilon)$ 411 nm (2.0×10^5), 521 nm (1.1×10^4), 615 nm (4.1×10^3) 646 nm (3.2×10^3 M^{-1} cm^{-1}).

Tetrasodium 5,10,15,20-tetrakis(2,6-difluoro-3-sulfonatophenyl)porphyrin nickel(II) (Na_4[Ni-F8P])

Tetrasodium 5,10,15,20-tetrakis(2,6-difluoro-3-sulfonatophenyl)-21*H*,23*H*-porphyrin·$4H_2O$ (124 mg, 0.10 mmol) and Milli-Q water (40 mL) were placed under N_2 in a 100 mL round-bottom flask equipped with a magnetic stirring bar and a condenser. A solution of Ni(II) acetate tetrahydrate (124 mg, 0.50 mmol) in Milli-Q water (10 mL) was added to the stirred solution and the mixture was refluxed for 12 h under N_2. After cooling to room temperature, the water was rotary evaporated and the residue was redissolved in cold methanol (15 mL), and filtered on a filter paper. After filtration, methanol was rotary-evaporated, the residue was redissolved in cold methanol (5 mL), the solution was filtered by filter paper and rotary-evaporated. The crude Na_4[Ni-F8P] product was finally passed through an Amberlite IR 120 Na^+ form ion exchange resin column (10 cm), washed with Milli-Q water and purified on a Sephadex-20H size exclusion chromatography column (eluent: methanol). Methanol was finally rotary evaporated and the solid dried in vacuo. Yield (115 mg, 90%); ^{1}H NMR (400 MHz, CD_3OD): δ = 9.03 – 8.99 (m, 8H; β-pyrrole-H), 8.45 – 8.38 (m, 4H; *p*-Ph-H), 7.56

– 7.50 ppm (m, 4H; *m*-Ph-H); ^{19}F NMR (471 MHz, CD_3OD): δ = -105.95 – -106.10 (m, 4F; *o*-F), -106.35 – -106.50 ppm (m, 4F; *o*-F); MS (ESI neg. ion): *m*/*z* calcd for $C_{44}H_{16}F_8N_4NiO_{12}S_4^{4-}$: 282.5 [*M*-4Na]$^{4-}$; found: 282.7; $C_{44}H_{16}F_8N_4NiO_{12}S_4^{4-}+H^+$: 377.0 [*M*-4Na+H]$^{3-}$; found: 377.2; $C_{44}H_{16}F_8N_4NiO_{12}S_4^{4-}+Na^+$: 384.3 [*M*-3Na]$^{3-}$; found: 384.6; $C_{44}H_{16}F_8N_4NiO_{12}S_4^{4-}+2Na^+$: 587.9 [*M*-2Na]$^{2-}$; found: 587.9; HRMS (ESI): *m*/*z* calcd for $C_{44}H_{20}F_8N_4NiO_{12}S_4Na^+$: 1156.9078 [*M*-3Na+4H]$^+$; found: 1156.9063; elemental analysis calcd (%) for $C_{44}H_{16}F_8N_4Na_4NiO_{12}S_4 \cdot 3H_2O$: C 41.37, H 1.74, N 4.39; found: C 41.53, H 1.68, N 4.36. UV-vis (H_2O): $\lambda_{max}(\varepsilon)$ 400 nm (3.1×10^5), 521 nm (1.9×10^4), 562 nm (7.9×10^3 M^{-1} cm^{-1}).

Tetrasodium 2,3,7,8,12,13,17,18-octafluoro-5,10,15-20-tetrakis(2,6-difluoro-3-sulfonatophenyl)porphyrin nickel(II) (Na_4[Ni-F16P])

Tetrasodium 2,3,7,8,12,13,17,18-octafluoro-5,10,15,20-tetrakis(2,6-difluoro-3-sulfonatophenyl)-21*H*,23*H*-porphyrin·$5H_2O$ (140 mg, 0.10 mmol) and Milli-Q water (40 mL) were placed under N_2 in a 100 mL round-bottom flask equipped with a magnetic stirring bar and a condenser. A solution of Ni(II) acetate tetrahydrate (124 mg, 0.50 mmol) in Milli-Q water (10 mL) was added to the stirred solution and the mixture was refluxed for 12 h under N_2. After cooling to room temperature, the water was rotary evaporated and the residue was redissolved in cold methanol (15 mL). After filtration over a filter paper, methanol was rotary-evaporated, the residue was redissolved in cold methanol (5 mL), and filtered by filter paper again. The filtrate was rotary-evaporated and the Na_4[Ni-F16P] complex was then passed through an Amberlite IR 120 Na^+ form ion exchange resin column (10 cm) and washed with Milli-Q water before being purified on Sephadex-20H size exclusion chromatography (eluent: methanol). Methanol was finally rotary evaporated and the solid dried in vacuo. Yield (124 mg, 86%); ^{1}H NMR (400 MHz, CD_3OD): δ = 8.89 (s, 4H; *p*-Ph-H), 8.00 ppm (s, 4H; *m*-Ph-H); ^{19}F NMR (471 MHz, CD_3OD): δ = -106.55 (s, 4F; *o*-F), -107.20 ppm (s, 4F; *o*-F) (the β-pyrrole-F atoms are not observed because of the nearby Ni^{2+} metal centre); MS (ESI neg. ion): *m*/*z* calcd for $C_{44}H_8F_{16}N_4NiO_{12}S_4^{4-}$: 318.5 [*M*-4Na]$^{4-}$; found: 318.9; $C_{44}H_8F_{16}N_4NiO_{12}S_4^{4-}+Na^+$: 432.3 [*M*-3Na]$^{3-}$; found: 432.3; $C_{44}H_8F_{16}N_4NiO_{12}S_4^{4-}+2Na^+$: 659.9 [*M*-2Na]$^{2-}$; found: 659.9; HRMS (ESI): *m*/*z* calcd for $C_{44}H_{12}F_{16}N_4NiO_{12}S_4Na^+$: 1300.8325 [*M*-3Na+4H]$^+$; found: 1300.8313; elemental analysis calcd (%) for $C_{44}H_8F_{16}N_4Na_4NiO_{12}S_4 \bullet 4H_2O$: C 36.71, H 1.12, N 3.89; found: C 36.41, H 0.85, N 3.85. UV-vis (H_2O): $\lambda_{max}(\varepsilon)$ 338 nm (3.9×10^4), 408 nm (3.0×10^5), 539 nm (1.9×10^4 M^{-1} cm^{-1})

2.4.3 Cyclic voltammetry and differential pulse voltammetry

Cyclic voltammetry (CV) and differential pulse voltammetry (DPV) measurements were performed using an Autolab PGstart10 potentiostat controlled by GPES4 software. All the CV and DPV measurements were recorded in 0.1 M sodium phosphate buffer (pH 7.0) using a three-compartment cell possessing a 0.07 cm^2 glassy-carbon electrode as the working electrode, Pt wire as the auxiliary electrode, Ag/AgCl (saturated KCl aq.) as the reference electrode, and $K_3[Fe(CN)_6]$ was added at the end of the measurements as internal standard ($E([Fe(CN)_6]^{3-}/[Fe(CN)_6]^{4-})$ = +0.361 V vs NHE).[62] Unless otherwise indicated, the potential was converted relative to NHE, the solutions were bubbled with high-purity argon for at least 30 min before analysis.

2.4.4 Photo-induced oxygen production

Photo-induced oxygen production from water was analyzed by a Clark oxygen electrode (Unisense OX-NP) controlled by x-5 UniAmp using Logger software. The irradiation source was an OSRAM Opto Semiconductors LD W5SM LED (λ_{irr} 450 nm, $\Delta\lambda_{1/2}$ = 25 nm) with water cooling. All the photochemical oxygen production measurements were carried out in a thermostated (298 K) photochemical reactor (total volume 25.0 mL). $[Ru(bpy)_3]Cl_2 \cdot 6H_2O$ (1.5 mg, 0.67 mM), the catalyst $[Ni\text{-}OMeP]^{4-}$, N $[Ni\text{-}MeP]^{4-}$, $[Ni\text{-}F8P]^{4-}$, $[Ni\text{-}F16P]^{4-}$, $[Ni\text{-}MPyP]^{4+}$, $[Ni\text{-}TMAP]^{4+}$ or Ni(II) acetate (0.05 mM), and $Na_2S_2O_8$ (35.7 mg, 50 mM) were added as solids in the reactor, and dissolved using sodium phosphate buffer (0.1 M, pH 7.0, 3.0 mL). Under constant stirring, the reactor was equipped with 1 rubber septum and 2 silicon septa in order to make an air-tight system (the set-up is shown in Figure AI.29). The Clark oxygen electrode was then inserted through the septum, to measure the dioxygen concentration in the head space (gas phase) of the photochemical reactor, and the whole system was deaerated by high-purity argon for at least 30 min. After removing the argon, the Clark oxygen electrode was calibrated by a four-time injection of 100 µL (4.46 µmol at 1 atm) of high-purity O_2 into the closed system, thereby limiting the overpressure to <2%; the calibration was adapted with the pressure change using Logger software, affording direct reading of the volume of dioxygen (µL) produced in the gas phase of the reactor (V_{gas} = 22.0 mL). Following calibration, the three used septa were replaced by new ones and Clark oxygen electrode was inserted into the system again. The system was degassed for 30 min with argon, then data recording was started, first keeping the system in the dark for another 30 min prior to starting light irradiation. Unless otherwise indicated, the data recording was stopped after 2.25 h of light irradiation.

2.4.5 Catalytic dioxygen production in the dark using $[Ru(bpy)_3](ClO_4)_3$ as chemical oxidant

Dark oxygen production from water using $[Ru(bpy)_3](ClO_4)_3$ as chemical oxidant was analyzed by a Clark oxygen electrode (Unisense OX-NP) controlled by x-5 UniAmp using Logger software. The $[Ru(bpy)_3](ClO_4)_3$ was synthesized according to published methods,[7,8] stored as solid under vacuum in the fridge, and used within two days. All the chemical oxygen production measurements were carried out in a thermostated (298 K) reactor (total volume 10.0 mL). Sodium phosphate buffer (0.1 M, pH 7.0, 4.5 mL) was added in the reactor and under constant stirring, the reactor was equipped with a rubber septum and two silicon septa in order to make an air-tight system. The Clark oxygen electrode was then inserted through the septum, to measure the dioxygen concentration in the head space (gas phase) of the reactor, and the whole system was deaerated by high-purity argon for at least 30 min. After removing the argon, the Clark oxygen electrode was calibrated by a four-time injection of 100 µL (4.46 µmol at 1 atm) of high-purity O_2 into the closed system, thereby limiting the overpressure to <8%; the calibration was adapted with the pressure change using Logger software, affording direct reading of the volume of dioxygen (µL) produced in the gas phase of the reactor (V_{gas} = 5.5 mL). The reactor was cleaned and dried after calibration, Na_4[Ni-F8P] was then added as solids in the reactor and dissolved using sodium phosphate buffer (0.1 M, pH 7.0, 4.0 mL), three new septa and Clark oxygen electrode were adapted to the system again. The system was degassed for 30 min with argon, at the same time 5 mL sodium phosphate buffer (0.1 M, pH 7.0) was degassed in a 10 mL flask equipped with a rubber septum, $[Ru(bpy)_3](ClO_4)_3$ was weighed as solid and stored in a Schlenk tube equipped with a rubber septum under argon. 0.5 mL degassed buffer was quickly transferred to the Schlenk tube to dissolve $[Ru(bpy)_3](ClO_4)_3$ and the resulting solution was injected to the reactor using an air-tight syringe, then the data recording was started. Unless otherwise indicated, the data recording was stopped after 40 min reaction.

2.4.6 Controlled-potential electrolysis equipped with a Clark electrode

Controlled-potential electrolysis (CPE) experiments coupled with a Clark oxygen electrode were CPE systems for oxygen evolution from water analysed by a Clark oxygen electrode (Unisense OX-NP) controlled by x-5 UniAmp using Logger software. The Clark oxygen electrode was two points calibrated in air saturated water and deaerated water before use. Different functional potentials were controlled by an Autolab PGstart10 potentiostat using GPES4 software to electrocatalyze OER using possessing a 0.07 cm^2 glassy-carbon electrode

as the working electrode, Pt wire as the auxiliary electrode, Ag/AgCl (saturated KCl aq.) as the reference electrode from a solution contains $[Ni\text{-}F8P]^{4-}$ or $[Ni\text{-}F16P]^{4-}$ (2.0 mM) in 0.1 M sodium phosphate buffer (pH 7.0, 6 mL) in a thermostated (298 K) electrochemical reactor (total volume 25 mL). A calibrated Clark oxygen electrode was set into the constant stirring solution to analyse the oxygen produced from the CPE system in aqueous phase. The whole system was deaerated by high-purity argon for at least 30 min and the top part of the reactor (gas phase) was always kept in argon atmosphere via argon flowing. Data recording of both systems started together, after electrolysis for 30 min, the two systems were stopped at the same time. Unless otherwise indicated, the data recording was stopped at the end of the 30 min electrolysis.

2.4.7 Calculation of Faradaic yield of CPE

The Faradaic yield (FY) was calculated using the amount of charge (It) passed in the electrochemical reactor, calculated by integrating the current (I) vs. electrolysis time (t), and the number of mol of dioxygen produced n_{O_2} according to the following equation:

$$FY = \frac{4 \times 96485 n_{O_2}}{\mathrm{It}}$$

in which n_{O_2} is the number of mol of dioxygen calculated from the concentration of the dioxygen produced in the CPE experiment as indicated by the calibrated Clark oxygen electrode in solution (μmol L^{-1}), times with the volume of CPE solution (6 mL); I is the current, t is the CPE time.

2.4.8 Dynamic Light Scattering

Dynamic Light scattering (DLS) was chosen to determine the numbers of particles in 0.1 M initial pH 7.0 sodium phosphate buffer solutions contain 0.67 mM $[Ru(bpy)_3]Cl_2$, 50 mM $Na_2S_2O_8$ and 0.05 mM 1) $[Ni\text{-}OMeP]^{4-}$, 2) $[Ni\text{-}MeP]^{4-}$, 3) $[Ni\text{-}F8P]^{4-}$, 4) $[Ni\text{-}F16P]^{4-}$, 5) $[Ni\text{-}MPyP]^{4+}$, 6) $[Ni\text{-}TMAP]^{4+}$, or 7) Ni(II) acetate and 8) 0.1 M initial pH 8.5 sodium phosphate buffer solution contains 0.67 mM $[Ru(bpy)_3]Cl_2$, 50 mM $Na_2S_2O_8$ and 0.05 mM Ni(II) acetate after 0, 0.5, 1.0, 1.5, 2.0 hours using a ZEN 1600 Zetasizer Nano instrument (Malvern Instruments Limited) operating with a 633 nm laser.

2.4.9 Turnover number determination

The turnover number (TON) of oxygen evolution was determined by a Clark oxygen electrode (Unisense OX-NP) controlled by x-5 UniAmp using Logger software. The amount of oxygen formed during 2.25 h illumination was used to calculate the TON. The TON were calculated from the oxygen production data by the following equation:

$$TON = \frac{n_{O_2}}{n_{cat}}$$

in which n_{O_2} is the number of mol of dioxygen calculated from the volume of the dioxygen produced in the photocatalytic experiment as indicated by the calibrated Clark oxygen electrode in the gas phase (µL), divided by 22.4 L/mol, and n_{cat} is the number of mol of nickel catalyst used in the photocatalytic experiment.

The maximum turnover frequency TOF_{max} (in min^{-1}) of photocatalytic oxygen evolution was obtained using Origin 9.1 software by 1) nonlinear curve fitting of the time evolution of the TON, starting at t = 30 min for photocatalytic reactions (category: Growth/Sigmoidal, function: logistic Fit); 2) calculating the first derivative TOF = f(t) using mathematics, differentiate, and 3) identify the maximum value TOF_{max} of TOF = f(t) (example of $[Ni\text{-}F8P]^{4-}$ see Figure 2.7).

The maximum O_2 evolution rate (in min^{-1}) of photocatalytic oxygen evolution was obtained using Origin 9.1 software by 1) nonlinear curve fitting of the time evolution of the mol of oxygen evolved, starting at t = 30 min and at t = 0 for dark oxygen production using $[Ru(bpy)_3](ClO_4)_3$ as chemical oxidant (category: Growth/Sigmoidal, function: logistic Fit); 2) calculating the first derivative O_2 evolution rate = f(t) using mathematics, differentiate, and 3) identify the maximum O_2 evolution rate value of O_2 evolution rate = f(t) (example for $[Ni\text{-}F8P]^{4-}$: see Figure 2.8).

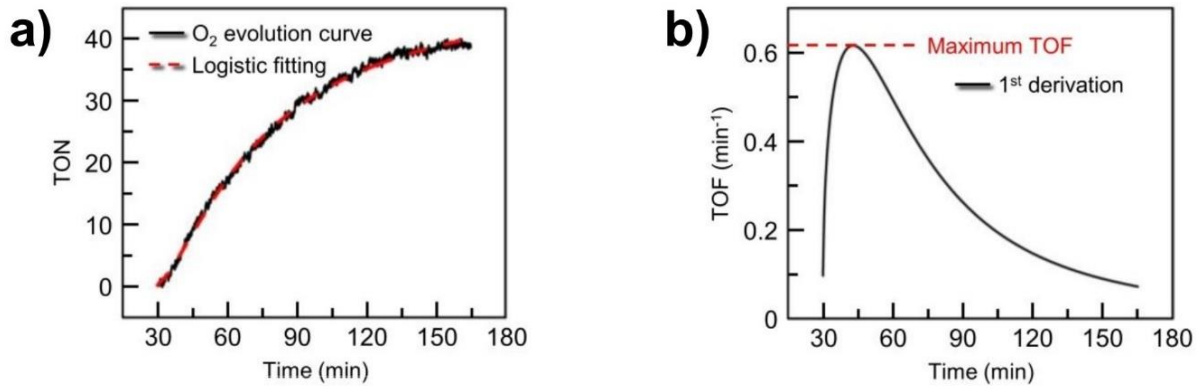

Figure 2.7 *Calculation of maximum turnover frequency of* $[Ni\text{-}F8P]^{4-}$.

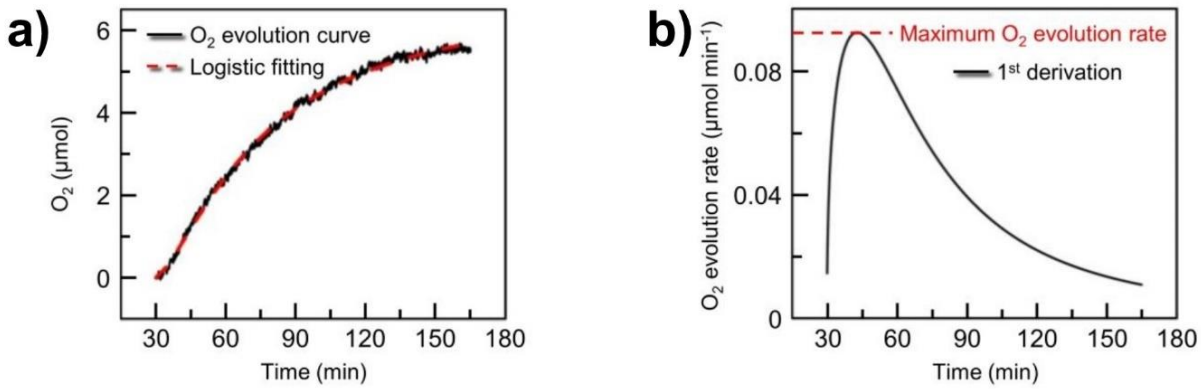

Figure 2.8 *Calculation of maximum O_2 evolution rate of [Ni-F8P]$^{4-}$.*

2.4.10 Calculation of photochemical O_2 production quantum yield

The O_2 generation quantum yield was calculated using the TOF_{max}, n_{cat} and the rate of photons absorption:

$$\varphi = \frac{2n_{cat}TOF_{max}}{60\Phi(1-10^{-A_e})(A_{PS}/A_e)}$$

in which TOF_{max} (min^{-1}) is the maximum turnover frequency of the photocatalytic oxygen evolution reaction, n_{cat} (in μmol) is the number of mol of nickel catalyst used in the photocatalytic experiment, Φ is the photon flux (μmol s^{-1}) determined by standard ferrioxalate actinometry (typically 1.05 μmol s^{-1}, 15.8 mW),[63] A_e is the total absorption of the photocatalytic solution at 450 nm (A_e>3), A_{PS} is the absorption of photosensitizer only in buffer at 450 nm (A_{PS}/A_e~1), and 60 is the number of seconds per minute. In this calculation we assumed 2 photons were needed for each molecule of O_2 produced.

2.5 Acknowledgement

C. Liu gratefully acknowledges the China Scholarship Council (CSC) for a personal grant (No. 201706360150).

2.6 References

[1] W. Zhang, W. Lai, R. Cao, *Chem. Rev.* **2017**, *117*, 3717-3797.

[2] D. K. Dogutan, D. G. Nocera, *Acc. Chem. Res.* **2019**, *52*, 3143-3148.

[3] B. Limburg, E. Bouwman, S. Bonnet, *Coord. Chem. Rev.* **2012**, *256*, 1451-1467.

[4] H.-C. Chen, D. G. H. Hetterscheid, R. M. Williams, J. I. van der Vlugt, J. N. H. Reek, A. M. Brouwer, *Energy Environ. Sci.* **2015**, *8*, 975-982.

[5] J. L. Fillol, Z. Codola, I. Garcia-Bosch, L. Gomez, J. J. Pla, M. Costas, *Nat. Chem.* **2011**, *3*, 807-813.

[6] M. D. Karkas, O. Verho, E. V. Johnston, B. Akermark, *Chem. Rev.* **2014**, *114*, 11863-12001.

[7] T. J. Meyer, M. V. Sheridan, B. D. Sherman, *Chem. Soc. Rev.* **2017**, *46*, 6148-6169.

[8] L. Duan, F. Bozoglian, S. Mandal, B. Stewart, T. Privalov, A. Llobet, L. Sun, *Nat. Chem.* **2012**, *4*, 418-423.

[9] N. Vereshchuk, R. Matheu, J. Benet-Buchholz, M. Pipelier, J. Lebreton, D. Dubreuil, A. Tessier, C. Gimbert-Surinach, M. Z. Ertem, A. Llobet, *J. Am. Chem. Soc.* **2020**, *142*, 5068-5077.

[10] Z. Li, N. A. Leed, N. M. Dickson-Karn, K. R. Dunbar, C. Turro, *Chem. Sci.* **2014**, *5*, 727-737.

[11] S. Ye, C. Ding, M. Liu, A. Wang, Q. Huang, C. Li, *Adv. Mater.* **2019**, *31*, 1902069.

[12] S. Dey, T. K. Todorova, M. Fontecave, V. Mougel, *Angew. Chem. Int. Ed.* **2020**, *59*,15726-15733.

[13] L. Duan, Y. Xu, P. Zhang, M. Wang, L. Sun, *Inorg. Chem.* **2010**, *49*, 209-215.

[14] N. Kaveevivitchai, R. Chitta, R. Zong, M. El Ojaimi, R. P. Thummel, *J. Am. Chem. Soc.* **2012**, *134*, 10721-10724.

[15] L. Tong, R. P. Thummel, *Chem. Sci.* **2016**, *7*, 6591-6603.

[16] D. J. Wasylenko, R. D. Palmer, C. P. Berlinguette, *Chem. Commun.* **2013**, *49*, 218-227.

[17] M. P. Santoni, G. La Ganga, V. Mollica Nardo, M. Natali, F. Puntoriero, F. Scandola, S. Campagna, *J. Am. Chem. Soc.* **2014**, *136*, 8189-8192.

[18] B. Schwarz, J. Forster, M. K. Goetz, D. Yucel, C. Berger, T. Jacob, C. Streb, *Angew. Chem. Int. Ed.* **2016**, *55*, 6329-6333.

[19] E. A. Karlsson, B. L. Lee, T. Akermark, E. V. Johnston, M. D. Karkas, J. Sun, O. Hansson, J. E. Backvall, B. Akermark, *Angew. Chem. Int. Ed.* **2011**, *50*, 11715-11718.

[20] C. Panda, J. Debgupta, D. Diaz Diaz, K. K. Singh, S. Sen Gupta, B. B. Dhar, *J. Am. Chem. Soc.* **2014**, *136*, 12273-12282.

[21] B. Das, A. Orthaber, S. Ott, A. Thapper, *ChemSusChem* **2016**, *9*, 1178-1186.

[22] Y. Zhao, J. Lin, Y. Liu, B. Ma, Y. Ding, M. Chen, *Chem. Commun.* **2015**, *51*, 17309-17312.

[23] T. Nakazono, A. R. Parent, K. Sakai, *Chem. Commun.* **2013**, *49*, 6325-6327.

[24] T. Nakazono, A. R. Parent, K. Sakai, *Chem. - Eur. J.* **2015**, *21*, 6723-6726.

[25] T. Nakazono, K. Sakai, *Dalton Trans.* **2016**, *45*, 12649-12652.

[26] M. A. Asraf, H. A. Younus, C. I. Ezugwu, A. Mehta, F. Verpoort, *Catal. Sci. Technol.* **2016**, *6*, 4271-4282.

[27] E. Pizzolato, M. Natali, B. Posocco, A. Montellano Lopez, I. Bazzan, M. Di Valentin, P. Galloni, V. Conte, M. Bonchio, F. Scandola, A. Sartorel, *Chem. Commun.* **2013**, *49*, 9941-9943.

[28] T. Ishizuka, A. Watanabe, H. Kotani, D. Hong, K. Satonaka, T. Wada, Y. Shiota, K. Yoshizawa, K. Ohara, K. Yamaguchi, S. Kato, S. Fukuzumi, T. Kojima, *Inorg. Chem.* **2016**, *55*, 1154-1164.

[29] N. S. McCool, D. M. Robinson, J. E. Sheats, G. C. Dismukes, *J. Am. Chem. Soc.* **2011**, *133*, 11446-11449.

[30] F. Evangelisti, R. Guttinger, R. More, S. Luber, G. R. Patzke, *J. Am. Chem. Soc.* **2013**, *135*, 18734-18737.

[31] S. Berardi, G. La Ganga, M. Natali, I. Bazzan, F. Puntoriero, A. Sartorel, F. Scandola, S. Campagna, M. Bonchio, *J. Am. Chem. Soc.* **2012**, *134*, 11104-11107.

[32] F. Song, R. More, M. Schilling, G. Smolentsev, N. Azzaroli, T. Fox, S. Luber, G. R. Patzke, *J. Am. Chem. Soc.* **2017**, *139*, 14198-14208.

[33] C.-F. Leung, S.-M. Ng, C.-C. Ko, W.-L. Man, J. Wu, L. Chen, T.-C. Lau, *Energy Environ. Sci.* **2012**, *5*.

[34] H. Y. Wang, E. Mijangos, S. Ott, A. Thapper, *Angew. Chem. Int. Ed.* **2014**, *53*, 14499-14502.

[35] J. Lin, X. Meng, M. Zheng, B. Ma, Y. Ding, *Appl. Catal., B* **2019**, *241*, 351-358.

[36] R. Terao, T. Nakazono, A. R. Parent, K. Sakai, *Chempluschem* **2016**, *81*, 1064-1067.

[37] R. J. Xiang, H. Y. Wang, Z. J. Xin, C. B. Li, Y. X. Lu, X. W. Gao, H. M. Sun, R. Cao, *Chem. - Eur. J.* **2016**, *22*, 1602-1607.

[38] M. Zhang, M. T. Zhang, C. Hou, Z. F. Ke, T. B. Lu, *Angew. Chem. Int. Ed.* **2014**, *53*, 13042-13048.

[39] Y. Han, Y. Wu, W. Lai, R. Cao, *Inorg. Chem.* **2015**, *54*, 5604-5613.

[40] J.-W. Wang, X.-Q. Zhang, H.-H. Huang, T.-B. Lu, *ChemCatChem* **2016**, *8*, 3287-3293.

[41] G. Chen, L. Chen, S. M. Ng, T. C. Lau, *ChemSusChem* **2014**, *7*, 127-134.

[42] L. Francàs, R. Matheu, E. Pastor, A. Reynal, S. Berardi, X. Sala, A. Llobet, J. R. Durrant, *ACS Catal.* **2017**, *7*, 5142-5150.

[43] U. S. Akhtar, E. L. Tae, Y. S. Chun, I. C. Hwang, K. B. Yoon, *ACS Catal.* **2016**, *6*, 8361-8369.

[44] W. C. Ellis, N. D. McDaniel, S. Bernhard, T. J. Collins, *J. Am. Chem. Soc.* **2010**, *132*, 10990-10991.

[45] B. Limburg, G. Laisne, E. Bouwman, S. Bonnet, *Chem. - Eur. J.* **2014**, *20*, 8965-8972.

[46] L. Huang, Y. Chen, G. Y. Gao, X. P. Zhang, *J. Org. Chem.* **2003**, *68*, 8179-8184.

[47] M. F. Zipplies, W. A. Lee, T. C. Bruice, *J. Am. Chem. Soc.* **1986**, *108*, 4433-4445.

[48] S. Nakagaki, F. L. Benedito, F. Wypych, *J. Mol. Catal. A.* **2004**, *217*, 121-131.

[49] J. C. Biffinger, H. Sun, A. P. Nelson, S. G. DiMagno, *Org. Biomol. Chem.* **2003**, *1*, 733-736.

[50] K. Bütje, K. Nakamoto, *Inorg. Chim. Acta* **1990**, *167*, 97-108.

[51] P. K. Ghosh, B. S. Brunschwig, M. Chou, C. Creutz, N. Sutin, *J. Am. Chem. Soc.* **1984**, *106*, 4772-4783.

[52] B. Limburg, E. Bouwman, S. Bonnet, *ACS Catal.* **2016**, *6*, 5273-5284.

[53] M. D. Karkas, B. Akermark, *Dalton Trans.* **2016**, *45*, 14421-14461.

[54] X. Zhang, Y. Y. Li, J. Jiang, R. Zhang, R. Z. Liao, M. Wang, *Inorg. Chem.* **2020**, *59*, 5424-5432.

[55] L. Huang, Y. Chen, G. Y. Gao, X. P. Zhang, *J. Org. Chem.* **2003**, *68*, 8179-8184.

[56] M. F. Zipplies, W. A. Lee, T. C. Bruice, *J. Am. Chem. Soc.* **1986**, *108*, 4433-4445.

[57] S. Nakagaki, F. L. Benedito, F. Wypych, *J. Mol. Catal. A.* **2004**, *217*, 121-131.

[58] J. C. Biffinger, H. Sun, A. P. Nelson, S. G. DiMagno, *Org. Biomol. Chem.* **2003**, *1*, 733-736.

[59] K. Bütje, K. Nakamoto, *Inorg. Chim. Acta* **1990**, *167*, 97-108.

[60] G. P. McDermott, P. Jones, N. W. Barnett, D. N. Donaldson, P. S. Francis, *Anal. Chem.* **2011**, *83*, 5453-5457.

[61] S. Fu, Y. Liu, Y. Ding, X. Du, F. Song, R. Xiang, B. Ma, *Chem. Commun.* **2014**, *50*, 2167-2169.

[62] R. C. J. Murray, P. A. Rock, *Electrochim. Acta* **1968**, *13*, 969-975.

[63] J.G.P. Calvert, J. N., *Chemical actinometer for the determination of ultraviolet light intensities. In Photochemistry.* Wiley and Sons, New York, **1967**, 780